Geophysical Research Letters

RESEARCH LETTER
10.1029/2024GL110764

Mid-Latitude Auroras and Energetic Particle Precipitation Occurred Unusually in a Moderate Magnetic Storm on 1 December 2023

Longxing Ma[1,2], Yiqun Yu[1,2], Xiaoqi Ding[1,2], Xiyu Liu[1,2], Depeng An[1,2], Chenlong Zhou[1,2], Jinbin Cao[1,2], and Kazuo Shiokawa[3]

[1]School of Space and Environment, Beihang University, Beijing, China, [2]Key Laboratory of Space Environment Monitoring and Information Processing, Ministry of Industry and Information Technology, Beijing, China, [3]Institute for Space-Earth Environmental Research, Nagoya University, Nagoya, Japan

Key Points:

- Mid-latitude auroras and energetic (E > 40 keV) particle precipitation are observed unusually during a moderate storm
- Energetic proton precipitation induced by Pc1/EMIC waves may contribute to the mid-latitude proton aurora
- Field-aligned currents emerge near at mid-latitudes, accompanied by significant magnetic perturbations

Supporting Information:

Supporting Information may be found in the online version of this article.

Correspondence to:

Y. Yu,
yiqunyu17@gmail.com

Citation:

Ma, L., Yu, Y., Ding, X., Liu, X., An, D., Zhou, C., et al. (2024). Mid-latitude auroras and energetic particle precipitation occurred unusually in a moderate magnetic storm on 1 December 2023. *Geophysical Research Letters*, *51*, e2024GL110764. https://doi.org/10.1029/2024GL110764

Received 17 JUL 2024
Accepted 1 SEP 2024

Abstract Mid-latitude auroras are conventionally generated during intense magnetic storms. However, mid-latitude auroras were observed by naked eyes at Beijing China (39°N, 116°E) unusually during a moderate storm event on 1 December 2023 with the minimum Sym-H index only ∼−120 nT. This study combines conjugative in-site and ground-based observations to analyze the auroras and underlying physical processes. Results indicate that both electron and proton auroras appeared at low latitudes. Electron auroras predominantly arise from low-energy electron precipitation, but proton auroras may be explained by energetic tens of keV proton precipitation. Pc1/EMIC waves are observed at low latitudes in the ionosphere, potentially accounting for mid-latitude proton auroras. Downward field-aligned currents (FACs) are also detected at low latitudes, producing significant magnetic perturbations. This study reveals the underlying ionospheric responses to the mid-latitude auroras to understand potential reasons for observing aurora at such mid-latitudes during a moderate storm.

Plain Language Summary Mid-latitude auroras were observed in Beijing, China unusually during a moderate storm event on 1 December 2023. Satellites and ground-based stations record obvious electron and proton auroras at low latitudes. The electron auroras are primarily caused by low-energy electron precipitation, while proton auroras are attributed to more energetic proton precipitation. Pc1/EMIC waves observed at low latitudes in the ionosphere could explain the appearance of proton auroras. Downward FACs are also observed at low latitudes, contributing to significant magnetic perturbations. This study analyzes potential reasons for the occurrence of mid-latitude auroras during a moderate storm.

1. Introduction

Auroras present impressive phenomena in the night sky, representing an important manifestation of magnetospheric-ionospheric interactions. The appearance of auroras in mid-latitude regions is commonly an indication of intense magnetic storms (Balan et al., 2019; Kataoka et al., 2017; Lockwood, 2015; Shiokawa et al., 2005). Recently on 1 December 2023, a moderately strong magnetic storm occurred and auroras were witnessed by naked eyes at Beijing China (at 39°N, 116°E) as shown in Figure 1a, lifting a strong wave of public interest. It is very rare in Chinese history to observe auroras as the country is basically located at low latitudes, far away from the high-latitude auroral oval. Only during extremely strong magnetic storms when the aurora expands equatorward may mid-latitude regions experience aurora phenomena. For example, in the most recent super storm on May 10–11, 2024, the Sym-H index reached below −400 nT and world-wide sightings of aurora were reported from unprecedentedly low-latitude regions (e.g., Boulder CO USA at 40°N; Beijing China at 39° N; Puerto Rico at 25°N; San Antonio Texas USA at 29°N). However, the storm event on 1 December 2023 was merely a moderate storm event. The minimum Sym-H index was only −120 nT and the maximum AE index was around 1,400 nT during the storm main phase when Beijing was located right in the dusk-to-midnight sector.

Motivated by this intriguing aurora event appeared at such a low latitude region during a moderate magnetic storm, we tend to analyze the underlying processes of the dusk-sector auroras and examine the impact of high-energy particle precipitation on the ionosphere. It is widely acknowledged that auroral activities are primarily attributed to precipitating electrons of a few to tens of keV (Lou et al., 2021; Newell et al., 2009; Su et al., 2010). Recent results indicate that the contribution of high-energy (several tens to a hundred keV) electron and proton

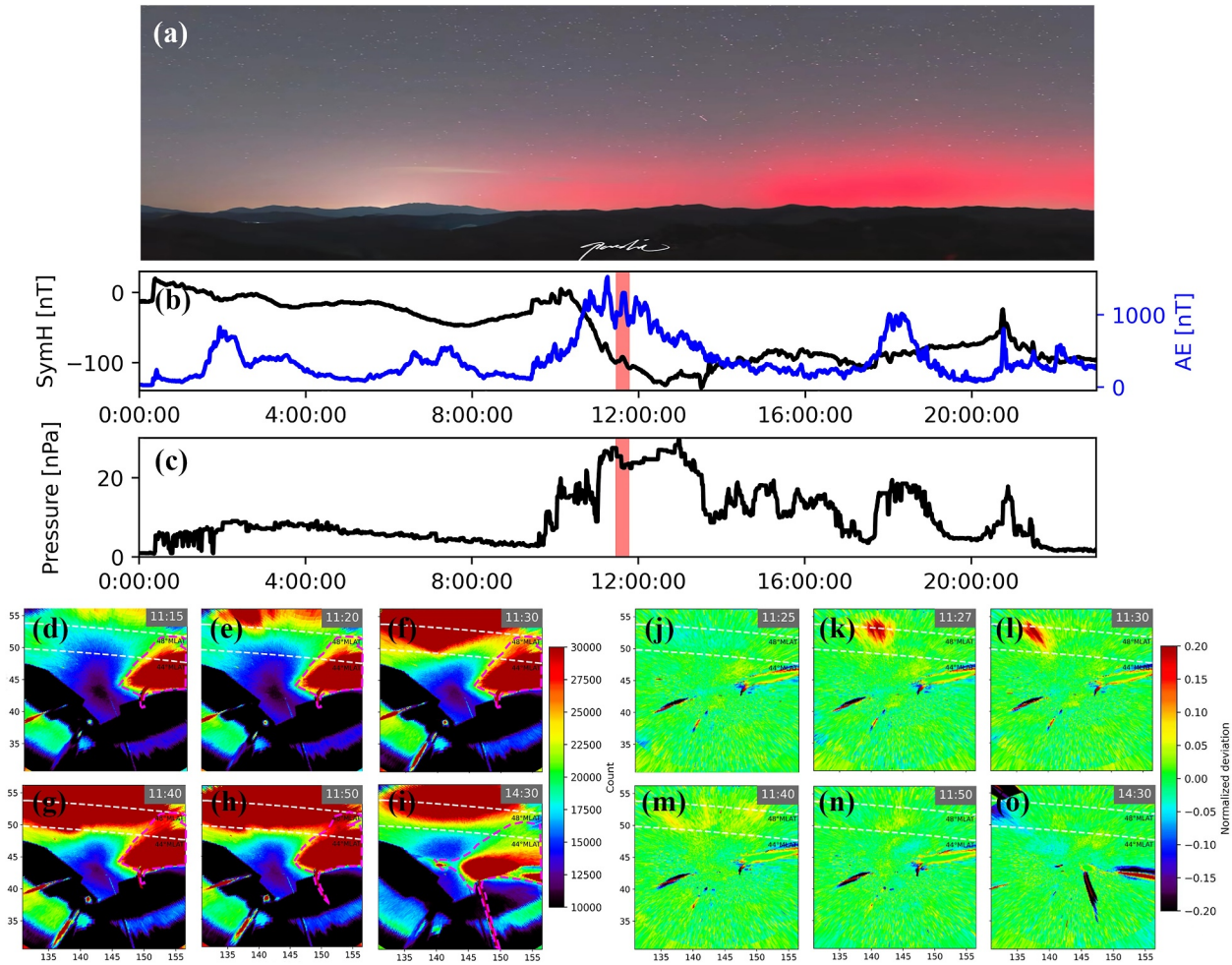

Figure 1. (a) Red aurora as seen from Huairou (39°N, 116° (e), Beijing, China around 11:30 UT on 1 December 2023, captured by a Nikon camera with 190 s exposure time. (Courtesy of Mr. Pu) (b) The Sym-H (black) and AE (blue) indexes during the storm event on 1 December 2023. The red region represents the first observations of mid-latitude auroras. (c) The variations of solar wind dynamic pressure. (d–o) Rikubetsu (RIK) all-sky imager (ASI) images at two different wavelengths: 630.0 nm emissions (d–i) at ∼200 km and 557.7 nm emissions (j–o) at ∼120 km from 11:15 UT to 14:30 UT in the geographic coordinate system. North (south) is oriented toward the top (bottom). White lines represent magnetic latitude obtained by the Geopack package and the T96 model. Yellow and red areas in panels (d–i) with counts greater than 22,000 represent the auroral region, mostly near the top edge. The black zone in the panels (d–i) is the shutter of RIK ASI. The persistent red emission of panels (d–i) encircled by pink dashed lines in the northeast corners may be contaminated by city lights, intense airglow, or reflection of the moon light by clouds. Note that (j–o) represent the deviation of 557.7 nm emission within a one-hour time window.

precipitation cannot be neglected. Tesema et al. (2020) found that energetic precipitating electrons can generate pulsating electron auroras and affect the near-Earth geospace environment. Besides electron auroras, proton auroras can be induced by energetic precipitating protons that are potentially driven by Electromagnetic Ion Cyclotron (EMIC) waves (Fuselier et al., 2004; Jordanova et al., 2007; Kim et al., 2021; Tian et al., 2023). Energetic ions can also precipitate via field line curvature (FLC) scattering when magnetic field lines are highly stretched, generating isotropic precipitation regions where the intensity of proton precipitating flux approaches that of the trapped flux. The equatorial boundary of the region is named isotropic boundary (IB) (Lvova et al., 2005; Ma et al., 2022; Sergeev et al., 1993; Yu et al., 2020).

In this study, a great number of facilities are fortunately available to provide remote-sensing images and in-site measurements. For example, the Rikubetsu (RIK) all-sky imager (ASI) in nearby Japan observes the evolution of electron auroras. The Defense Meteorological Satellite Program (DMSP) observes proton auroras at dusk. NOAA/Polar Operational Environmental Satellites (POES) and DMSP satellites detect variations of particle precipitation. Swarm satellites record high-precision magnetic field perturbations in the ionosphere. The Active Magnetosphere and Planetary Electrodynamics Response Experiment (AMPERE) provides the global

distribution of field-aligned currents (FACs) before and during the event. Ground-based magnetometers record magnetic field perturbations under the aurora. All of these observations can contribute to a deep understanding of the features and origins of the mid-latitude auroras and the effects of energetic particle precipitation.

2. Data Set Descriptions

The RIK station (43.5°N, 143.8°E) in Japan is equipped with an all sky airglow/aurora imager, which can capture aurora images of various wavelengths. To determine the evolution of auroras, we use 557.7 (green) and 630.0 (red) nm auroral images observed at RIK (Shiokawa et al., 2005). The aurora emitted by secondary electrons via proton-neutral collisions is captured by 557.7 nm auroral images, and electron aurora emitted by precipitating electrons can be recorded by 630.0 nm auroral images. Both proton and electron precipitation contribute to the 557.7 nm auroras. To distinguish proton auroras from electron auroras, we further utilize the auroral images from DMSP to identify proton auroras.

The DMSP F17 satellite was launched in 2006 into a circular polar orbit with an altitude of approximately 840 km and an inclination of 98.9°. Equipped with the SSJ5 particle detector, the spacecraft measures fluxes of ions and electrons ranging from 30 to 30 keV across 19 logarithmically spaced channels at a frequency of once per second (Hardy, 1984). The spacecraft also carries the Special Sensor Ultraviolet Spectrographic Imager (SSUSI) (Paxton et al., 1992, 1993). With approximately 14 passes per day, SSUSI records far-ultraviolet emissions using a scanning imaging spectrograph, with its observational mirror positioned perpendicular to the satellite track. The resolution of the SSUSI imagery is 16 × 156 pixels, covering approximately one-third to one-half of the auroral oval. Although SSUSI offers five spectral channels in its imaging mode, the HI Lyman α (121.6 nm) channel is of particular interest in this study, which can be associated with proton precipitation to discriminate proton aurora.

Data on more energetic (E > 40 keV) proton and electron precipitation can be acquired from NOAA/POES satellites. These satellites belong to the category of low-altitude sun-synchronous polar orbit satellites, with an orbital altitude of approximately 800 km and a period of about 102 min. Observations of precipitating and trapped flux originate from the Space Environment Monitor-2 (SEM-2) (Evans & Greer, 2000), which offers a temporal resolution of 2 s. The detector consists of two telescopes for precipitating particles (0° telescope) and trapped particles (90° telescope), respectively. The proton telescopes have six channels (P1–P6), while the electron telescopes contain three energy channels (E1–E3). The P6 channel is designed to measure proton fluxes with E > 6.9 MeV, yet it suffers from significant contamination by relativistic electrons with E > 0.8 MeV. This study primarily utilizes data from E1–E3 and P1–P3 channels.

Swarm mission, consisting of three spacecraft, was launched into a high-inclination (87.5°) low-Earth orbit on 22 November 2013 (Friis-Christensen et al., 2006). Swarm-A and Swarm-C fly side by side at the same altitude (∼450 km) and Swarm-B in a slightly higher altitude orbit (∼530 km). The orbit period is about 93 min but slightly different between A, C, and B, resulting in changes in latitude separation along the orbit. Each satellite is equipped with a high-precision vector magnetometer with a sampling rate of 50 Hz and a resolution of 0.01 nT to measure the three-dimensional geomagnetic field. We employ a previously introduced methodology for identifying ionospheric Pc1/EMIC waves (Wang et al., 2019, 2022). Firstly, the second-order Savitzky-Golay smoothing filter is applied to acquire background fields. Subsequently, the magnetic field perturbation is obtained by subtracting the corresponding background field from the raw data, and then transformed into the mean field-aligned (MFA) coordinate system. Finally, Fourier transform analysis is conducted on the magnetic perturbation to obtain the wave spectrum. The time window of Fourier transform spans 256 data points (16 s), with an overlapping window of 128 points (8 s).

Furthermore, the AMPERE provides global maps of FAC system every 10 min (Anderson et al., 2014), allowing for continuous monitoring of the global distribution of FACs in the ionosphere. Ground magnetic perturbations in this event are recorded by fluxgate magnetometers at Paratunka station (52.9°N, 158.2°E) with a sampling of 1 Hz and a resolution is 0.1 nT. All of the above-mentioned observations will be utilized to analyze the potential origin and ionospheric impact of the mid-latitude aurora event in the 1 December 2023 moderate storm.

3. Results

Figures 1b and 1c illustrate the evolution of Sym-H, AE indexes and solar wind dynamic pressure of the storm. During the storm main phase from 10:30 UT on, the minimum Sym-H index reached about −120 nT and the

maximum AE index was around 1,400 nT. The maximum solar wind dynamic pressure was up to 27.46 nPa. The RIK ASI at 43.5°N in Japan detected clear auroral emissions in the north part of the field-of-view (FOV) around 11:30 UT when the Sym-H index was approximately −100 nT and the AE index around 1,100 nT.

3.1. Mid-Latitude Auroras and Precipitation

Figure 1a shows red auroras as seen from Huairou (39°N, 116°E), Beijing, China around 11:30 UT on 1 December 2023. Assuming the captured aurora altitude is approximately 400 km and the elevation angle from Beijing is about 15°, it is estimated that red auroras occurred at 13.5° in latitude north of Beijing. Thus, the estimated magnetic latitude (MLAT) of red auroras is about 47.5° (Beijing's MLAT is about 34° calculated by International Geomagnetic Reference Field (IGRF)). This estimate aligns closely with the 630.0 nm emission count captured by RIK ASI in Figures 1d–1i. The black zone in the images is the shutter of the imager. White lines represent magnetic latitudes inferred by the Geopack package using IGRF and T96 models. The mid-latitude 630.0 nm emission by electron precipitation is not observed until 11:20 UT (Figure 1e). It firstly appears at 49° MLAT, and then gradually expands and shifts westward and equatorward, predominantly concentrated above 46° MLAT regions. After 11:30 UT, the notable 630.0 nm emission gradually shifts to lower latitudes. Around 14:30 UT, it weakens and retreats toward higher latitudes before fading away. On the other hand, Figures 1j–1o illustrate the deviation of 557.7 nm emission within a one-hour time window, which helps to demonstrate the variations in emission during the time interval (Supporting Information Figures S1a–S1f in Supporting Information S1) shows the counts of 557.7 nm emission). Figure 1k shows intense emissions initially near 49° MLAT at the north edge. Subsequently, this intense emission shifts westward and to lower latitudes, corresponding to 46° MLAT. Around 11:40 UT, it weakens and retreats toward higher latitudes before fading away from the FOV.

Since 557.7 nm emission is susceptible to electron precipitation, an accurate representation of proton aurora is challenging. Alternatively, we analyze the 121.6 nm ultraviolet emission captured by the DMSP SSUSI instrument. The emission at this wavelength is associated with proton precipitation (Paxton et al., 1992, 1993). Figures 2a and 2b indicate proton auroras at 121.6 nm in the altitude-adjusted corrected geomagnetic (AACGM) coordinate system before and during the event, respectively. The blue dashed line represents the equatorward boundary of the aurora oval, which is skewed toward low latitudes in the night. The proton aurora is primarily confined in the regions of 65° MLAT before the event at 10:15 UT (Figure 2a). But it manifests a pronounced equatorward shift during the event at 11:54 UT by approximately 10° with a remarkable amplification in intensity (Figure 2b). It is then mainly located within 50°–55° MLAT, consistent with the auroral characteristics detected via the RIK ASI 557.7 nm emissions. Meanwhile, the DMSP SSJ5 particle detector records the variation of low-energy particle precipitating flux, as shown in Figures 2c–2f. Before the event (Figures 2c and 2d), low-energy (< 30 keV) proton and electron precipitation with weak intensity are localized around 67° but during the event the precipitation occurs at a much lower latitude (Figures 2e and 2f). The precipitating electron flux substantially increases by an order of magnitude as compared to the pre-event. These low-energy electrons at lower latitudes are likely the cause of the mid-latitude electron aurora. It is noted that, although the mid-latitude proton precipitating flux of $E < 1$ keV also experiences an increase in the second trajectory, that at higher energies (e.g., $1 < E < 30$ keV) exhibits little change compared to pre-event.

Fortunately, both the NOAA/POES and Swarm satellites traverse the region of interest before and during the event, respectively, capturing the variations of high-energy ($E > 40$ keV) particle precipitation and magnetic perturbations near the mid-latitude auroras from 10:00 to 12:00 UT. The trajectories are displayed by colored curves in Figures 2a and 2b. During the time interval of interest when both satellites observed particle precipitation and waves during the event, both satellites are within the FOV of RIK, providing a great opportunity for conjugate study. Specifically, the METOP-1 satellite successively traverses the mid-latitude region before and during the appearance of mid-latitude aurora. Figures 3a–3d show the energetic ($E > 40$ keV) proton and electron fluxes recorded along the two trajectories. It is found that both energetic proton and electron fluxes exhibit significant enhancements and the equatorward boundary of the intense precipitation notably shifts toward lower latitudes during the event, reaching approximately 49°–50° MLAT around 11:30 UT, where and when the auroral variations are observed by RIK and DMSP.

The proton IB, the equatorward boundary where the trapped proton flux (dashed lines) and precipitating proton flux (solid lines) are comparable, is identified in the flux observations and marked by vertical lines for different energy channels. The iB is firstly observed at approximately 58° MLAT around 9:50 UT, and it shifts

10.1029/2024GL110764

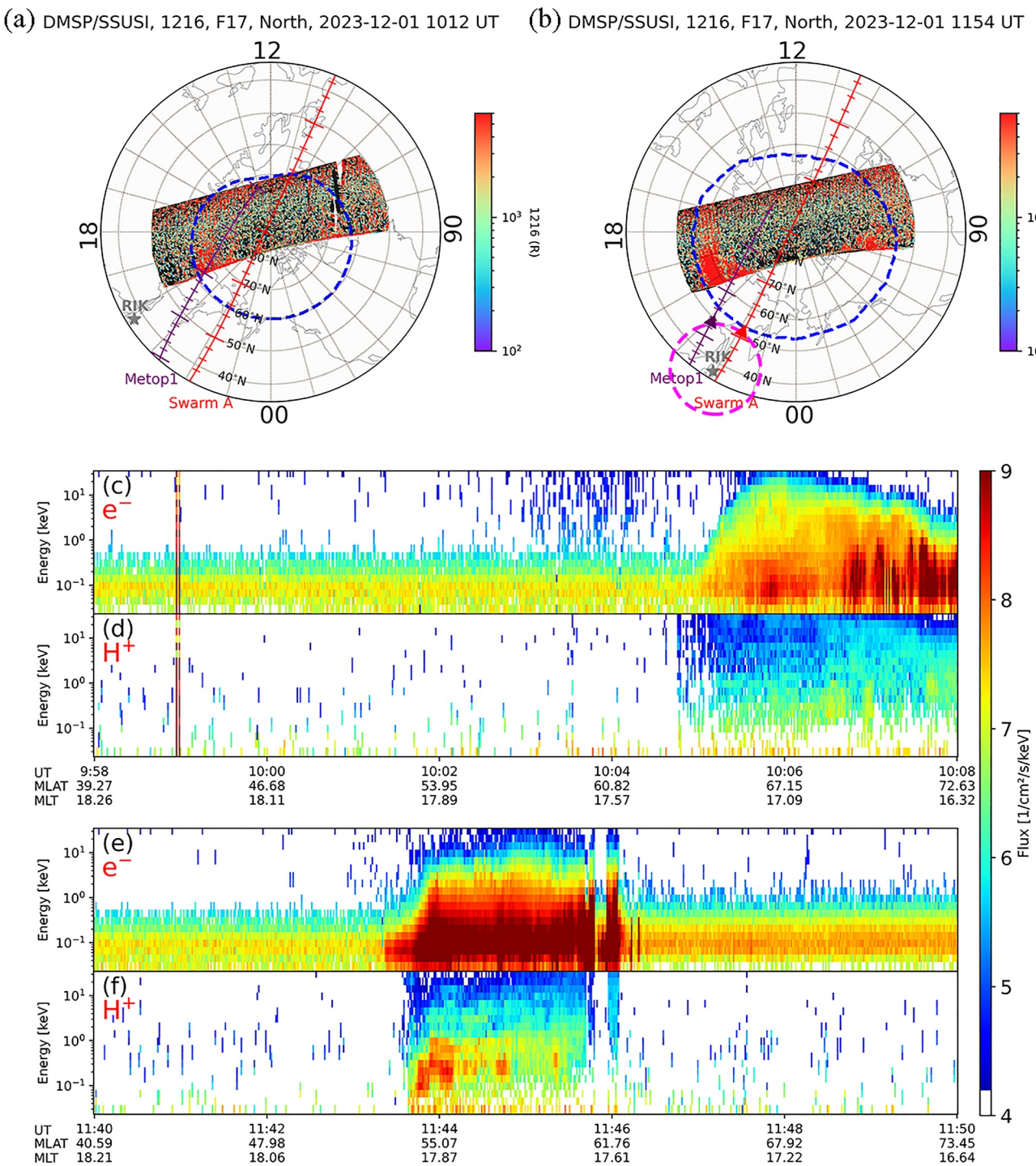

Figure 2. (a–b) 126.1 nm auroral images from the Special Sensor Ultraviolet Spectrographic Imager instrument on Defense Meteorological Satellite Program (DMSP) F17 in the AACGM coordinate system. The purple and red lines represent the trajectories of METOP-1 and Swarm-A satellites, respectively. The purple triangle indicates the latitudes of particle precipitation first detected by METOP-1, while the red triangle represents the latitudes of EMIC waves first observed by Swarm-A. The pink dashed circle represents the field-of-view of Rikubetsu. The blue dashed lines represent the equatorward boundaries of auroral oval. (c–d) E < 30 keV precipitating electron (c) and proton (d) fluxes obtained by DMSP F17 before the event. (e–f) E < 30 keV precipitating electron (e) and proton (f) fluxes obtained by DMSP F17 during the event.

10.1029/2024GL110764

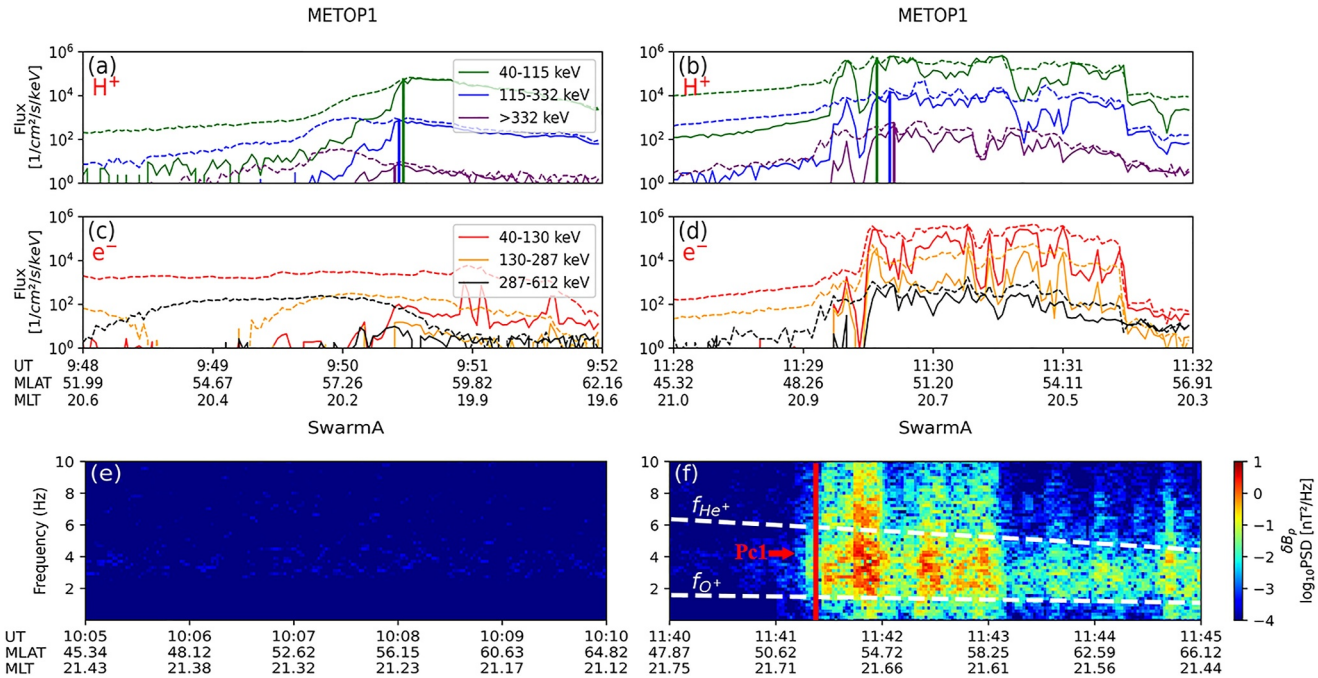

Figure 3. (a–b) E > 40 keV precipitating and trapped proton fluxes captured by METOP-1 before and during the event. (c–d) E > 40 keV precipitating and trapped electron fluxes obtained by METOP-1 before and during the event. Solid and dashed lines denote particle precipitating flux and trapped flux, respectively. (e–f) The dynamic spectrum of B_p magnetic field disturbances measured by Swarm-A before and during the event. The upper and lower white dashed lines represent the He^+ and O^+ gyrofrequencies at the equatorial position where the ground stations are mapped to. The red vertical line indicates the equatorward boundary of broadband pulsations. The disturbances to the left (marked by the red arrow) correspond to Pc1 waves.

equatorward to around 50° MLAT by 11:30 UT. At this time, the proton aurora also reaches its lowest latitude, as seen in Figure 1. Previous studies proposed that the formation of IB is generally attributed to FLC scattering (Lvova et al., 2005; Yu et al., 2020), although debates still exist as EMIC wave can also induce significant proton precipitation and cause IB (Sergeev et al., 2015). Nevertheless, the two mechanisms can be distinguished. It is believed that the latitude of the IB formed by FLC scattering generally exhibits an energy-latitude dispersion (Ma et al., 2022; Sergeev et al., 2015). That is, the IB is located more equatorward for higher energy flux. This is clearly true in Figure 3a around 9:50 UT. However, an anomalous energy-latitude dispersion is observed around 11:30 UT, as shown in Figure 3b. The IB is located at a higher latitude for higher energy protons. Such a reversed relation in proton fluxes has been previously reported and was proposed to be an indication of EMIC waves (Liang et al., 2014; Sergeev et al., 2015). In other words, the transient increase of energetic proton precipitation may be a result of EMIC wave scattering during the disturbed time.

We further conduct the Fast Fourier Transform (FFT) analysis on the parallel component of magnetic fields detected by the Swarm-A satellite. The frequency spectrum shows little disturbances before the event (Figure 3e), but during the event (Figure 3f)), it reveals strong broadband magnetic fluctuations. These broadband magnetic spectra are observed over the auroral oval where magnetic field fluctuations are primarily induced by Region 1 and 2 FACs. The two white lines represent He^+ and O^+ gyrofrequencies at the equator mapped onto the satellite altitude along magnetic field lines using the IGRF and T96 magnetic models. It is noted that a protruded He-band Pc1/EMIC wave at ∼2–6 Hz emerged equatorward of the broadband spectra (separated by the red vertical line), at low latitudes around 51° at 11:41 UT. Although none of magnetospheric satellites are in the possible source region to detect the original EMIC waves, the clear Pc1/EMIC waves in the ionospheric altitude and the anomalous energy-latitude dispersion in the IB locations suggest that EMIC waves are excited and are likely responsible for the proton aurora observed at mid latitudes.

In addition, the event is accompanied by transient enhancements of electron precipitating fluxes at tens to a few hundred keV (see Figure 3d). This could be driven by whistler waves as well as EMIC waves. The whistler wave can interact with electrons below 100 keV (see Tsai et al., 2022; Zhang et al., 2022, 2023), while EMIC waves are known to interact with energetic electrons at sub-relativistic energy (Capannolo et al., 2021; Miyoshi et al., 2008).

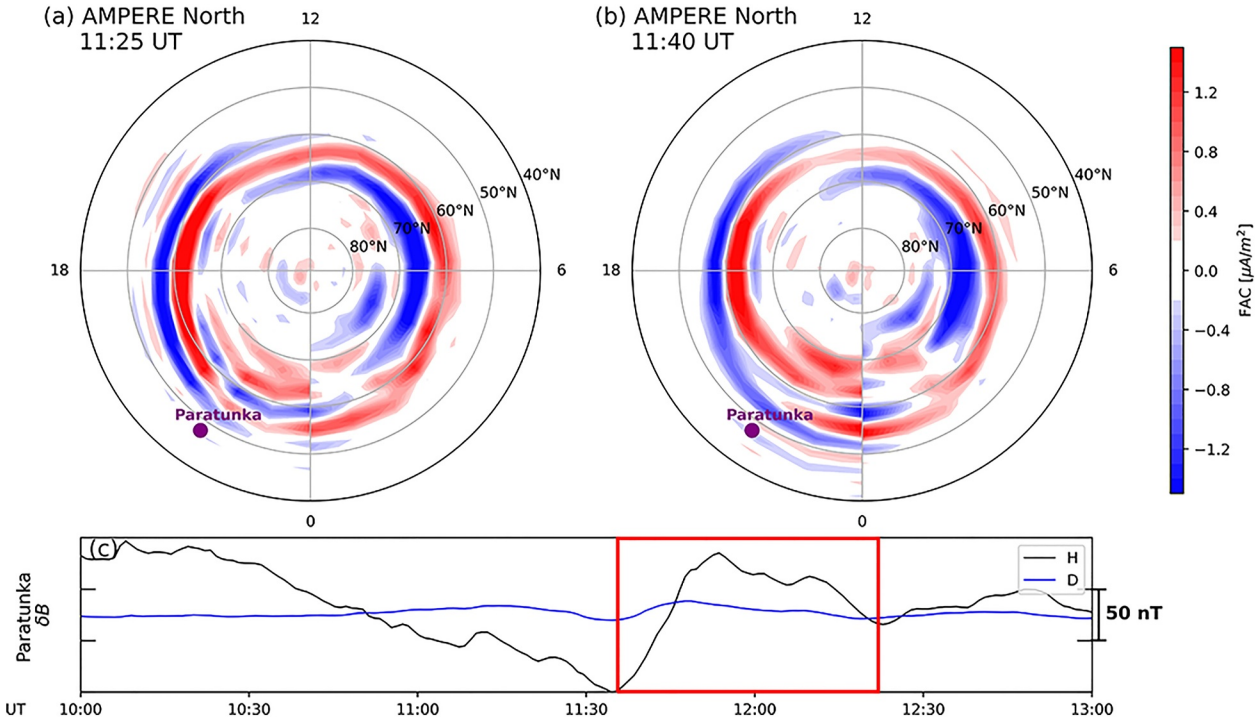

Figure 4. (a–b) AMPERE global field-aligned current (FAC) maps in the AACGM coordinate system derived from magnetic field perturbations measured by Iridium satellites. Positive (negative) FAC represents the upward (downward) flowing current. Purple points represent the location of the ground-based Paratunka station. (c) The magnetic perturbation of H and D components recorded at the Paratunka station.

Again as no magnetospheric satellites are located at relevant source regions to observe the whistler waves, we could only speculate that multiple waves may be triggered and result in significant flux enhancement in both electrons and protons.

3.2. FACs and Magnetic Field Disturbances

We further investigate the ionospheric disturbances following the mid-latitude particle precipitation. To analyze the spatial evolution of FAC, we employ AMPERE to obtain the global distribution of FAC before and during the event, as shown in Figures 4a and 4b. The distribution of FAC at 11:40 UT is skewed toward lower latitudes in the night, corresponding to the observations of mid-latitude auroras. After comparing the two snapshots, it is found that a new pair of FACs appeared in mid-latitude regions around Magnetic local time (MLT) = 22 at 11:40 UT, flowing into the ionosphere at 47° MLAT and out at 50° MLAT. The alternating occurrence of positive and negative FACs in mid latitudes is associated with the simultaneous presence of ion and electron precipitation.

Meanwhile, the nearby Paratunka ground magnetometer station records variations in the H (northward) and D (eastward) geomagnetic components (Figure 4c). As denoted in the red box, both H and D components are enhanced intensely by approximately 80 and 20 nT from 11:40 to 11:50 UT, respectively. These enhancements imply that there appears a significant downward FAC equatorward as well as to the east of the station, which is confirmed by the AMPERE map. As shown in Figure 4b), the downward FAC south of Paratunka can induce northward and eastward magnetic field perturbations at Paratunka. Given the magnitude of downward FAC from AMPERE at an altitude of 780 km (AACGM coordinate system), we estimate the magnetic field perturbation to be about 30 nT, consistent with the order of magnitude in the H and D components in Figure 4c from 11:40 to 11:50 UT. At this time, the substorm remains intense as shown in Figure 1. A substantial amount of particles is injected into the inner magnetosphere during the substorm, accompanied by the excitation of fluctuations, facilitating energetic particle transport energy to the ionosphere, resulting in notable downward FACs. Such a downward current, carrying energy deposits from the magnetosphere, could largely disturb the mid-latitude ionosphere.

4. Discussion and Conclusions

Mid-latitude auroras have traditionally been regarded to be associated with intense magnetic storms. However, recently during a moderate storm event occurred on 1 December 2023 with the minimum Sym-H index ~ -120 nT, auroral phenomena were observed by naked eyes at mid-latitude regions in East Asia, such as Beijing China at $\sim 39°$N. Although the global disturbances are not large enough to be categorized as an intense magnetic storm, significant changes are clearly detected in the mid-latitude dusk-to-midnight sector where East Asia is right located.

The RIK ASI provides comprehensive records of the complete process from the appearance to the equatorward migration and eventual disappearance of both proton and electron auroras. The DSMP satellites record the evolution of proton auroras moving from high latitude to low latitude and provide variations in low-energy particle precipitation fluxes before and during the event. It is suggested that electron auroras are primarily induced by low-energy ($E < 30$ keV) electron precipitation. METOP-1 satellite at Low-Earth-orbit reveals a significant enhancement and equatorward shift of energetic ($E > 40$ keV) proton precipitation, likely induced by EMIC waves excited from the magnetosphere. The high-precision magnetic field data from Swarm-A provide evidence of helium-band EMIC waves at low latitudes, although high-latitude broadband spectra are influenced by FACs in the aurora oval. These results suggest that the mid-latitude proton aurora may be attributed to energetic proton precipitation caused by EMIC wave scattering. Although auroras have been conventionally accounted for by low-energy particle precipitation, the significant contribution of energetic proton precipitation to the auroras during this event cannot be ignored. Simultaneously, AMPERE observes a newly emerged pair of FACs in mid-latitude regions around MLT = 22 close to the high-energy particle precipitation. The H and D components of magnetic perturbations detected by a nearby ground-based Paratunka station indicate a substantial enhancement in both northward and eastward geomagnetic fields, consistent with the newly emerged FACs. All of these remote-sensing, in situ, and ground-based observations together provide a comprehensive picture of the mid-latitude aurora phenomena and the underlying physical processes.

Isotropic boundary distribution exhibits distinct reversed energy-latitude dispersion during the appearance of mid-latitude proton auroras, suggesting that energetic proton precipitation may be accounted for by EMIC wave scattering. Results from high-precision magnetic field data captured by Swarm-A further confirm the presence of Pc1/EMIC fluctuations. However, significant wave leakage, harmonic interference, or potential influence from FAC obscures the EMIC wave characteristics, necessitating further analysis. Furthermore, as depicted in Figures 3a and 3b, the energetic proton precipitation shifts from approximately 58° in high-latitude to nearly 50°. Before the event, the IB distribution maintains a normal energy-latitude relationship, suggesting the absence of EMIC waves. Based on observations from other trajectories of METOP-1 (not shown), the evolution of energetic proton precipitation regions before this event could be attributed to the stretching of magnetic field lines caused by solar wind compression. Subsequently, during the event, high-energy protons are scattered by EMIC waves into the ionosphere, leading to an equatorward shift of proton precipitation and expansion of mid-latitude proton aurora. Meanwhile, METOP-1 detects transient enhancements in electron precipitation fluxes within the 40–130 keV range at low latitudes, likely driven by whistler waves in the magnetosphere. Therefore, the occurrence of mid-latitude auroras during a moderate magnetic storm may result from a combined influence of intense EMIC and other waves.

As a final note, the occurrence of mid-latitude auroras coincides with the peak of solar wind dynamic pressure as illustrated in Figure 1c. Intense solar wind pressure can significantly compress magnetic field lines and alter their configurations. To quantify the compressed extent of magnetic field lines and the relationship between sudden enhancements in solar wind pressure and the appearance of mid-latitude auroras, we use the IGRF and T96 magnetic models to compare the ionospheric latitudes corresponding to a fixed region in the magnetospheric equatorial plane ($L = 2$–5.5, MLT = 22) before and during the auroral event. Compared to the pre-event, there is a significant trend of magnetic field lines in the inner magnetosphere shifting toward lower latitudes around 11:40 UT as shown in Figure S2a in Supporting Information S1. This results in the extension of low-energy electron precipitation into lower latitude regions, making it possible for red auroras to be observed in Beijing. Furthermore, there is a substorm eruption as shown in Figure 1b around 11:10 UT, which injects a large amount of hot plasma into the low L region, enhancing the anisotropy and triggering the excitation of EMIC/Pc1 waves (Tian et al., 2022; Zhu et al., 2021). Around 11:40 UT, Swarm-A detects intense quasi-parallel EMIC/Pc1 waves as shown in Figure S2b in Supporting Information S1, which supply precipitating particles down to the upper

atmosphere. Meanwhile, the dynamic pressure reaches ~25 nPa, around the peak value, resulting in a most-compressed configuration, so the mid-latitude magnetic field lines on the nightside may be stretched to the lowest latitudes, allowing energetic protons scattered by EMIC/Pc1 waves to precipitate into lower latitude regions. Since Beijing is located near 22 MLT at this time, a brief observation of the auroral event is possible at Beijing. According to the observations by RIK, the electron auroras are located at lower latitudes and more prominent than proton auroras. So the observed red auroras in Beijing could be electron auroras. Note that the IGRF and T96 magnetic models may underestimate the extent of low-latitude movement of magnetic field lines, the actual movement toward lower latitudes due to solar wind compression may be more significant than indicated by the model results. Recently, Kataoka et al. (2024) reported the red aurora in Japan during the same event and discussed the role of high solar wind density and pressure in the generation of the aurora. Our study utilizes combined observational data and simulation results to explain the potential mechanisms behind the auroras observed in Beijing, suggesting the equatorward movement of magnetic field lines compressed by solar wind dynamic pressure and wave-particle interactions together contribute to the mid-latitude auroras during a moderate magnetic storm.

Data Availability Statement

The authors thank the Kyoto, Japan World Data Center System (JWDCS (2023)) for providing the Sym-H, AE indexes and solar wind dynamic pressure and the Institute for Space-Earth Environmental Research (ISEE), Nagoya University for providing the all-sky airglow images of RIK (RIK (2023)). DMSP auroral data and low-energy particle flux are archived at SSUSI (2023) and SSJ5 (2023). The Swarm data are freely accessible at Swarm (2023). Data from NOAA/POES spacecraft are available from POES (2023). The AMPERE data can be obtained from AMPERE (2023). The Paratunka data are available from Paratunka (2023).

Acknowledgments
This work is supported by the National Natural Science Foundation of China (NSFC) Grants 42350710793 and 41821003, and by the Fundamental Research Funds for the Central Universities. We acknowledge Dr. Pu from Beijing Institute of Technology for his aurora photos in Beijing.

References

AMPERE. (2023). Active magnetosphere and planetary electrodynamics response experiment (AMPERE) data archive [Dataset]. *Ampere*. Retrieved from http://ampere.jhuapl.edu/

Anderson, B., Korth, H., Waters, C., Green, D., Merkin, V., Barnes, R., & Dyrud, L. (2014). Development of large-scale birkeland currents determined from the active magnetosphere and planetary electrodynamics response experiment. *Geophysical Research Letters*, *41*(9), 3017–3025. https://doi.org/10.1002/2014gl059941

Balan, N., Zhang, Q.-H., Shiokawa, K., Skoug, R., Xing, Z., Tulasi Ram, S., & Otsuka, Y. (2019). IPSDST of DST storms applied to ionosphere-thermosphere storms and low-latitude aurora. *Journal of Geophysical Research: Space Physics*, *124*(11), 9552–9565. https://doi.org/10.1029/2019ja027080

Capannolo, L., Li, W., Spence, H., Johnson, A., Shumko, M., Sample, J., & Klumpar, D. (2021). Energetic electron precipitation observed by firebird-ii potentially driven by emic waves: Location, extent, and energy range from a multievent analysis. *Geophysical Research Letters*, *48*(5), e2020GL091564. https://doi.org/10.1029/2020gl091564

Evans, D., & Greer, M. (2000). Polar orbiting environmental satellite space environment monitor.

Friis-Christensen, E., Lühr, H., & Hulot, G. (2006). Swarm: A constellation to study the earth's magnetic field. *Earth Planets and Space*, *58*(4), 351–358. https://doi.org/10.1186/bf03351933

Fuselier, S., Gary, S., Thomsen, M., Claflin, E., Hubert, B., Sandel, B., & Immel, T. (2004). Generation of transient dayside subauroral proton precipitation. *Journal of Geophysical Research*, *109*(A12), A12227. https://doi.org/10.1029/2004ja010393

Hardy, D. A. (1984). Precipitating electron and ion detectors (SSJ/4) for the block 5d/flights 6-10 DMSP satellites: Calibration and data presentation. *AFGL-TR-84-0317*.

Jordanova, V. K., Spasojevic, M., & Thomsen, M. (2007). Modeling the electromagnetic ion cyclotron wave-induced formation of detached subauroral proton arcs. *Journal of Geophysical Research*, *112*(A8), A08209. https://doi.org/10.1029/2006ja012215

JWDCS. (2023). Japan world data center system (JWDCS) [Dataset]. *KYOTO, JWDCS*. Retrieved from https://wdc.kugi.kyoto-u.ac.jp/aeasy

Kataoka, R., Isobe, H., Hayakawa, H., Tamazawa, H., Kawamura, A. D., Miyahara, H., et al. (2017). Historical space weather monitoring of prolonged aurora activities in Japan and in China. *Space Weather*, *15*(2), 392–402. https://doi.org/10.1002/2016sw001493

Kataoka, R., Miyoshi, Y., Shiokawa, K., Nishitani, N., Keika, K., Amano, T., & Seki, K. (2024). Magnetic storm-time red aurora as seen from Hokkaido, Japan on December 1, 2023 associated with high-density solar wind. *Authorea Preprints*.

Kim, H., Shiokawa, K., Park, J., Miyoshi, Y., Miyashita, Y., Stolle, C., et al. (2021). Isolated proton aurora driven by EMIC PC1 wave: PWING, swarm, and NOAA POES multi-instrument observations. *Geophysical Research Letters*, *48*(18), e2021GL095090. https://doi.org/10.1029/2021gl095090

Liang, J., Donovan, E., Ni, B., Yue, C., Jiang, F., & Angelopoulos, V. (2014). On an energy-latitude dispersion pattern of ion precipitation potentially associated with magnetospheric emic waves. *Journal of Geophysical Research: Space Physics*, *119*(10), 8137–8160. https://doi.org/10.1002/2014ja020226

Lockwood, M. (2015). An arch in the UK: A new catalogue of auroral observations made in the British Isles and Ireland. *Astrononmy and Geophysics*, *56*, 25.

Lou, Y., Cao, X., Ni, B., Tu, W., Gu, X., Fu, S., et al. (2021). Diffuse auroral electron scattering by electrostatic electron cyclotron harmonic waves in the dayside magnetosphere. *Geophysical Research Letters*, *48*(5), e2020GL092208. https://doi.org/10.1029/2020gl092208

Lvova, E., Sergeev, V., & Bagautdinova, G. (2005). Statistical study of the proton isotropy boundary. In *Annales geophysicae*, (Vol. 23(4), pp. 1311–1316). Copernicus Publications Göttingen. https://doi.org/10.5194/angeo-23-1311-2005

Ma, L., Yu, Y., Tian, X., & Cao, J. (2022). An empirical model of the proton isotropic boundary (IB). *Journal of Geophysical Research: Space Physics*, *127*(9), e2022JA030843. https://doi.org/10.1029/2022ja030843

Miyoshi, Y., Sakaguchi, K., Shiokawa, K., Evans, D., Albert, J., Connors, M., & Jordanova, V. (2008). Precipitation of radiation belt electrons by emic waves, observed from ground and space. *Geophysical Research Letters*, *35*(23), L23101. https://doi.org/10.1029/2008gl035727

Newell, P., Sotirelis, T., & Wing, S. (2009). Diffuse, monoenergetic, and broadband aurora: The global precipitation budget. *Journal of Geophysical Research*, *114*(A9), A09207. https://doi.org/10.1029/2009ja014326

Paratunka. (2023). Paratunka data archive. [Dataset]. *Paratunka*. Retrieved from https://imag-data.bgs.ac.uk/gin_v1/ginforms2

Paxton, L. J., Meng, C.-I., Fountain, G. H., Ogorzalek, B. S., Darlington, E. H., Gary, S. A., et al. (1992). Special sensor ultraviolet spectrographic imager: An instrument description. In *Instrumentation for planetary and terrestrial atmospheric remote sensing* (Vol. 1745, pp. 2–15). SPIE. https://doi.org/10.1117/12.60595

Paxton, L. J., Meng, C.-I., Fountain, G. H., Ogorzalek, B. S., Darlington, E. H., Gary, S. A., et al. (1993). Ssusi: Horizon-to-horizon and limb-viewing spectrographic imager for remote sensing of environmental parameters. In *Ultraviolet technology IV* (Vol. 1764, pp. 161–176). SPIE. https://doi.org/10.1117/12.140846

POES. (2023). Polar operational environmental satellites (POES) data archive [Dataset]. *POES*. Retrieved from https://cdaweb.gsfc.nasa.gov/

RIK. (2023). Rikubetsu (RIK) data archive [Dataset]. *RIK*. Retrieved from https://ergsc.isee.nagoya-u.ac.jp/data/ergsc/ground/camera/omti/asi/rik/

Sergeev, V., Chernyaeva, S., Apatenkov, S., Ganushkina, N., & Dubyagin, S. (2015). Energy–latitude dispersion patterns near the isotropy boundaries of energetic protons. In *Annales geophysicae* (Vol. 33, pp. 1059–1070). Copernicus GmbH.

Sergeev, V., Malkov, M., & Mursula, K. (1993). Testing the isotropic boundary algorithm method to evaluate the magnetic field configuration in the tail. *Journal of Geophysical Research*, *98*(A5), 7609–7620. https://doi.org/10.1029/92ja02587

Shiokawa, K., Ogawa, T., & Kamide, Y. (2005). Low-latitude auroras observed in Japan: 1999–2004. *Journal of Geophysical Research*, *110*(A5). https://doi.org/10.1029/2004ja010706

SSJ5. (2023). Defense meteorological satellite program (dmsp) ssj5 data archive [Dataset]. *SSJ5, DMSP*. Retrieved from http://cedar.openmadrigal.org/list/

SSUSI. (2023). Defense meteorological satellite program (dmsp) ssusi data archive [Dataset]. *SSUSI, DMSP*. Retrieved from https://ssusi.jhuapl.edu/

Su, Z., Zheng, H., & Wang, S. (2010). A parametric study on the diffuse auroral precipitation by resonant interaction with whistler mode chorus. *Journal of Geophysical Research*, *115*(A5), A05219. https://doi.org/10.1029/2009ja014759

Swarm. (2023). Swarm data archive [Dataset]. *Swarm*. Retrieved from https://swarm-diss.eo.esa.int/

Tesema, F., Partamies, N., Tyssøy, H. N., Kero, A., & Smith-Johnsen, C. (2020). Observations of electron precipitation during pulsating aurora and its chemical impact. *Journal of Geophysical Research: Space Physics*, *125*(6), e2019JA027713. https://doi.org/10.1029/2019ja027713

Tian, X., Yu, Y., Gong, F., Ma, L., Cao, J., Solomon, S. C., et al. (2023). Ionospheric modulation by emic wave-driven proton precipitation: Observations and simulations. *Journal of Geophysical Research: Space Physics*, *128*(1), e2022JA030983. https://doi.org/10.1029/2022ja030983

Tian, X., Yu, Y., Zhu, M., Ma, L., Cao, J., Pr, S., et al. (2022). Effects of emic wave-driven proton precipitation on the ionosphere. *Journal of Geophysical Research: Space Physics*, *127*(2), e2021JA030101. https://doi.org/10.1029/2021ja030101

Tsai, E., Artemyev, A., Zhang, X.-J., & Angelopoulos, V. (2022). Relativistic electron precipitation driven by nonlinear resonance with whistler-mode waves. *Journal of Geophysical Research: Space Physics*, *127*(5), e2022JA030338. https://doi.org/10.1029/2022ja030338

Wang, H., He, Y., & Lühr, H. (2022). Analysis of ionospheric compressional waves and electron density oscillation during storm periods using swarm observations. *Journal of Geophysical Research: Space Physics*, *127*(8), e2022JA030409. https://doi.org/10.1029/2022ja030409

Wang, H., He, Y., Lühr, H., Kistler, L., Saikin, A., Lund, E., & Ma, S. (2019). Storm time emic waves observed by swarm and Van Allen probe satellites. *Journal of Geophysical Research: Space Physics*, *124*(1), 293–312. https://doi.org/10.1029/2018ja026299

Yu, Y., Tian, X., & Jordanova, V. K. (2020). The effects of field line curvature (flc) scattering on ring current dynamics and isotropic boundary. *Journal of Geophysical Research: Space Physics*, *125*(8), e2020JA027830. https://doi.org/10.1029/2020ja027830

Zhang, X.-J., Angelopoulos, V., Artemyev, A., Mourenas, D., Agapitov, O., Tsai, E., & Wilkins, C. (2023). Temporal scales of electron precipitation driven by whistler-mode waves. *Journal of Geophysical Research: Space Physics*, *128*(1), e2022JA031087. https://doi.org/10.1029/2022ja031087

Zhang, X.-J., Angelopoulos, V., Mourenas, D., Artemyev, A., Tsai, E., & Wilkins, C. (2022). Characteristics of electron microburst precipitation based on high-resolution elfin measurements. *Journal of Geophysical Research: Space Physics*, *127*(5), e2022JA030509. https://doi.org/10.1029/2022ja030509

Zhu, M., Yu, Y., & Jordanova, V. K. (2021). Simulating the effects of warm o+ ions on the growth of electromagnetic ion cyclotron (EMIC) waves. *Journal of Atmospheric and Solar-Terrestrial Physics*, *224*, 105737. https://doi.org/10.1016/j.jastp.2021.105737